Editors' Suggestion

Self-aligning recirculated crossed optical dipole trap for lithium atoms

Ming Lian, Maximillian Mrozek-McCourt, Christopher K. Angyal, Dadbeh Shaddel, Zachary J. Blogg, John R. Griffin,* Ian Crawley,† and Ariel T. Sommer‡

Department of Physics, Lehigh University, Bethlehem, Pennsylvania 18015, USA

(Received 25 June 2024; revised 18 November 2024; accepted 21 November 2024; published 27 December 2024)

Crossed optical dipole traps (ODTs) provide three-dimensional confinement of cold atoms and other optically trappable particles. However, the need to maintain the intersection of the two trapping beams poses strict requirements on alignment stability and limits the ability to move the trap. Here we demonstrate a crossed ODT design that features inherent stability of the beam crossing, allowing the trap to move and remain aligned. The trap consists of a single high-power laser beam, imaged back onto itself at an angle to form a crossed trap. Self-aligning behavior results from employing an imaging system with positive magnification tuned precisely to unity. We employ laser-cooled samples of ^{6}Li atoms to demonstrate that the trap remains well aligned over a 4.3-mm travel range along an axis approximately perpendicular to the plane containing the crossed beams. Our scheme can be applied to bring an atomic cloud held in a crossed ODT close to a surface or field source for various applications in quantum simulation, sensing, and information processing.

DOI: 10.1103/PhysRevA.110.063121

I. INTRODUCTION

Advances in techniques for cooling and trapping atomic gases have enabled tremendous progress over the past few decades in quantum simulation, quantum sensing, and quantum information processing. Control over the position of an atomic sample often plays a crucial role in cold-atom experiments. In quantum simulation, quantum gas microscopy relies on positioning atoms close to a high-numerical-aperture microscope objective [1–3]. Proximity of atoms to an rf antenna can be beneficial for experiments employing strong rf magnetic fields to engineer atomic properties and observe novel phenomena [4–6]. Long-range transport enables an atomic cloud to be moved to a different section of a vacuum system in complex setups [7–14]. In quantum sensing applications, sensitive detection of magnetic [15,16] and electric [17] fields from materials depends on the distance of atoms to the material surface [18,19]. Quantum simulation, sensing, and information processing with hybrid atomic systems often rely on bringing an atomic sample to the vicinity of an optical device such as a high-finesse cavity [20–22] or hollow-core fiber [23–25].

Methods to trap and position clouds of neutral atoms employ magnetic forces, optical forces, or a combination. All-optical trapping offers the advantages of faster evaporative cooling [9,26–31], the ability to trap magnetically untrappable states [32], the freedom to tune the magnetic field independently [33], and improved optical access [10,14]. In a single-beam optical dipole trap (ODT), dynamic trap positioning has been implemented in the transverse directions using a variety of methods [34–38] and in the axial direction by lens translation [8,10,12] or with a focus-tunable lens [39,40]. The axial confinement in an all-optical single-beam ODT is relatively weak, particularly when using larger beam diameters to achieve a large trap volume. A crossed ODT solves this problem by forming a trap at the intersection of two beams that cross at an angle. The angle of the crossing controls the aspect ratio of the trap [41], and the additional degrees of freedom of the second beam provide further control over the trapping potential [27–29,42,43]. Crossed ODTs are therefore widely used for capturing atoms from a laser-cooled cloud. However, compared to the single-beam case, crossed traps are sensitive to misalignment, and tuning the position of a crossed ODT requires both beams to move in a coordinated way to keep them intersected.

One method to keep a crossed ODT aligned during repositioning is to send two parallel beams through a shared lens that focuses the beams to the same point, forming a small-angle crossed trap at the focus [9,44]. Translation of the lens allows long-range transport of the trap along the axial direction. Another approach allows transverse displacement by splitting a beam after an acouso-optic deflector and sending the two beams through symmetric paths [45]. However, to make maximal use of available laser power from a single light source, experiments often form a crossed ODT from a single recirculated beam that intersects with itself, giving twice the trap depth [28,46–50]. The question then arises whether a recirculated crossed ODT can be implemented that remains aligned as its position is tuned.

In this paper, we show how to produce a recirculated crossed ODT that remains aligned while the trap is repositioned, despite drift in the source beam. In

*Present address: AO Sense, Inc., Fremont, California 94538, USA.
†Present address: Nokia Bell Labs, Murray Hill, New Jersey 07974, USA.
‡Contact author: ats317@lehigh.edu

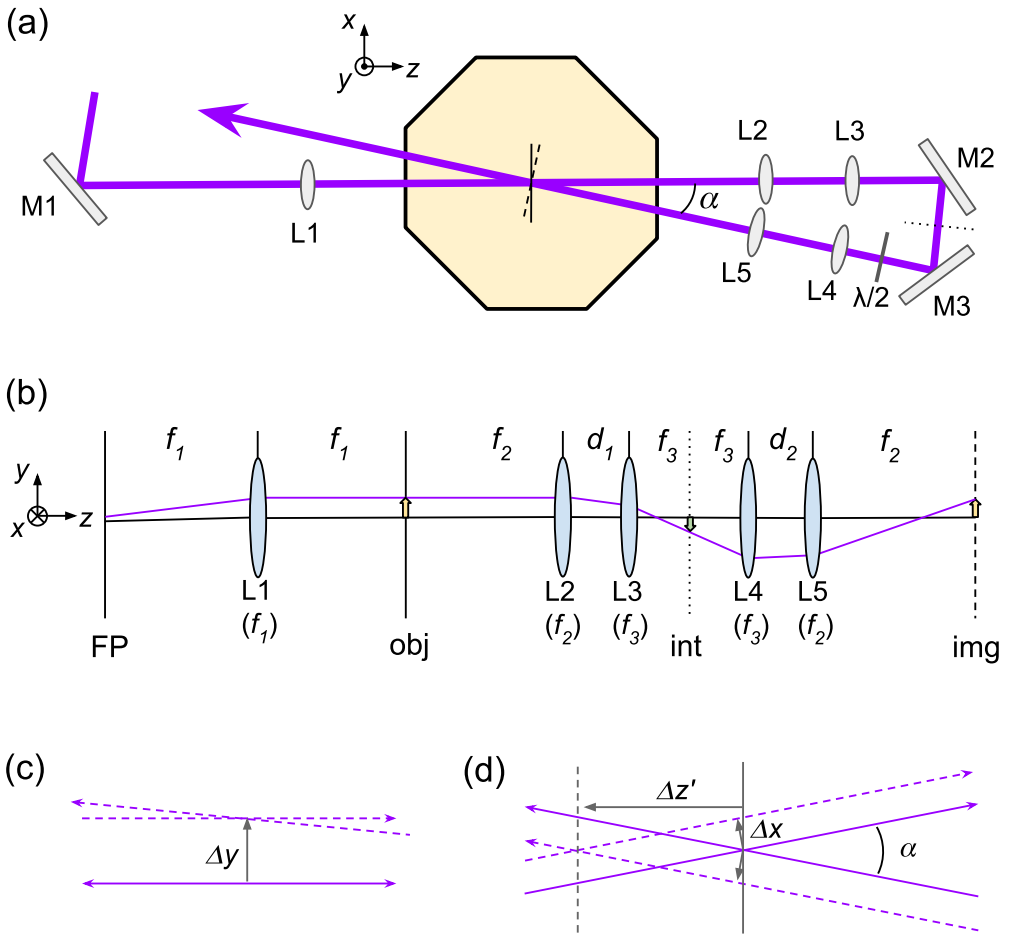

FIG. 1. (a) Schematic of the self-aligning recirculated crossed ODT (top-down view) showing the trap beam passing twice through the vacuum chamber (octagon). The short solid line in the chamber represents the horizontal axis in the object plane (x), while the dashed line represents the horizontal axis of the image plane ($\bar{x}$). The two planes share a common y axis (out of the page). The dotted line between M2 and M3 is the intermediate focal plane. (b) Unfolded lens system in the vertical y-z plane, showing the locations of the Fourier plane (FP), object plane (obj), intermediate focal plane (int), and image plane (img). The latter three are indicated by solid, dotted, and dashed lines, respectively, to match the schematic in (a). The purple line shows the path of the trapping beam after a vertical tilt of M1. (c) Vertical adjustment of M1 moves the first- and second-pass foci by the same amount Δy when the vertical magnification is tuned to 1. (d) Horizontal adjustment of M1 causes the two trapping beams to move away from one another symmetrically. The beams continue to intersect if they lie in the horizontal plane, which happens for $y = 0$ and for nonzero y in a setup where $d_1 + d_2 = 2(f_2 + f_3)$. The crossing point moves along the longitudinal (z') axis of the trap.

particular, our method allows tuning the position of the trap over several millimeters along the axis perpendicular to the plane containing the crossed beams. We implement the self-aligning crossed ODT design in an apparatus intended for studying strongly interacting Fermi gases out of equilibrium [51] to improve trap stability and to facilitate tuning the trap position relative to a magnetic-field saddle point. To demonstrate the self-aligning property of the trap, we manually vary its position and employ a sample of ^{6}Li atoms to show that the trapping beams maintain their intersection.

In Sec. II we describe the operating principle of our self-aligning crossed ODT. In Sec. III we describe a numerical-ray-tracing analysis of the design. In Sec. IV we describe the experimental setup. In Sec. V we report experimental results demonstrating our setup with a gas of ^{6}Li atoms. In Sec. VI we conclude.

II. OPERATING PRINCIPLE OF THE SELF-ALIGNING TRAP

A. General case of a recirculated crossed ODT

We consider a crossed ODT formed in the horizontal (xz) plane, as shown in Fig. 1. A single beam passes twice through a vacuum chamber, intersecting itself at an angle α to form a crossed trap. Both passes of the beam are focused at the crossing point, where atoms are trapped.

The focus of the second-pass beam is formed using a lens system that images the first-pass focal plane (object plane) onto the second-pass focal plane (image plane). A paraxial ray in the object plane is mapped onto a ray in the image plane by a formal 2×2 ray matrix:

$$\begin{pmatrix} \bar{\boldsymbol{\rho}} \\ d\bar{\boldsymbol{\rho}}/d\bar{z} \end{pmatrix}_{\text{im}} = \begin{pmatrix} A & B \\ C & D \end{pmatrix} \begin{pmatrix} \boldsymbol{\rho} \\ d\boldsymbol{\rho}/dz \end{pmatrix}_{\text{ob}}. \tag{1}$$

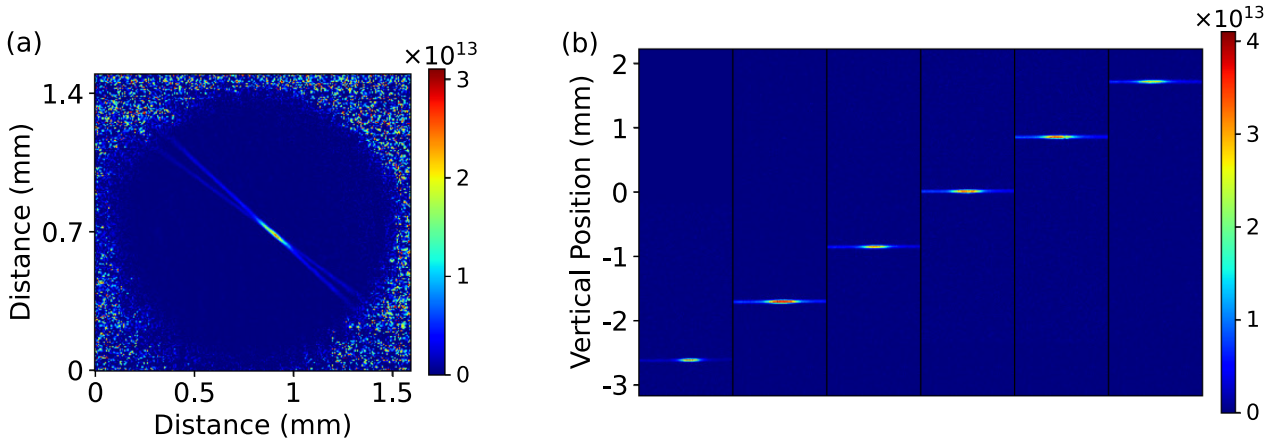

FIG. 2. (a) Top-down view of the crossed ODT. (b) Side view of the crossed ODT after moving the trap from $y = 0$ to different vertical positions. The second-pass focus is imaged precisely back onto the first-pass focus, leaving the trap intact and able to hold atoms. The color scales in (a) and (b) indicate the integrated column density of atoms in the second-lowest hyperfine state ($|2\rangle$) in units of m^{-2}, obtained from absorption imaging.

Here $\boldsymbol{\rho} = (x, y)$ are transverse coordinates, and z is the longitudinal coordinate in the object coordinate system. The barred variables $(\bar{x}, \bar{y}, \bar{z})$ refer to the image coordinate system. The subscripts "ob" and "im" refer to object and image points, respectively. The image plane is defined to minimize the beam-spot size including aberrations but is close to the paraxial image plane where $B = 0$. Due to the folding of the optical path by mirrors M2 and M3, the object and image planes intersect at an angle of $\pi - \alpha$. We can relate the coordinates of a point P in the two coordinate systems by a rotation matrix:

$$\begin{pmatrix} \bar{x} \\ \bar{y} \\ \bar{z} \end{pmatrix}_{\mathrm{P}} = \begin{pmatrix} -\cos\alpha & 0 & -\sin\alpha \\ 0 & 1 & 0 \\ \sin\alpha & 0 & -\cos\alpha \end{pmatrix} \begin{pmatrix} x \\ y \\ z \end{pmatrix}_{\mathrm{P}}. \tag{2}$$

For small α, then, $x_{\mathrm{im}} \approx -\bar{x}_{\mathrm{im}} = -Ax_{\mathrm{ob}}$, so that, in a fixed coordinate system, the horizontal magnification is approximately $-A$. Meanwhile, for any α, $y_{\mathrm{im}} = \bar{y}_{\mathrm{im}} = Ay_{\mathrm{ob}}$, so the vertical magnification is A in both global and local coordinates.

A conventional method of forming a recirculated crossed ODT employs a pair of lenses to refocus the beam [28,46–50] and gives $A < 0$. In a typical setup, the lenses have equal focal lengths and are each located one focal length from the atoms, so $A \approx -1$. The vertical magnification is then negative, so that a vertical movement of the first-pass focus causes an opposite movement of the second-pass focus. The alignment of the trap is therefore sensitive to drift in the pointing of the first-pass beam. Furthermore, any attempt to reposition the trap along the axis perpendicular to the crossed beams (i.e., vertically) causes the trap to lose alignment.

B. Self-aligning configuration

In this work, we study an alternative setup that allows repositioning of the trap without loss of alignment, in contrast to the conventional implementation described at the end of the previous section. In our setup, shown in Figs. 1(a) and 1(b), the imaging system that refocuses the second-pass beam consists of two subsystems, each with a negative vertical magnification, resulting in a net-positive vertical magnification $A > 0$ that we tune close to 1. The first subsystem consists of lenses L2 and L3, with focal lengths f_2 and f_3, respectively, separated by a distance d_1, and refocuses the beam onto an intermediate focal plane with a magnification of $-f_3/f_2$. The second subsystem consists of lenses L4 and L5, with focal lengths f_3 and f_2, respectively, separated by a distance d_2, and images the intermediate focal plane onto the final image plane in the vacuum chamber, with a magnification of $-f_2/f_3$. The net magnification is then 1. The ray matrix appearing in (1) becomes approximately

$$\begin{pmatrix} A & B \\ C & D \end{pmatrix} = \begin{pmatrix} 1 & 0 \\ \dfrac{2(f_2 + f_3) - (d_1 + d_2)}{f_2^2} & 1 \end{pmatrix}. \tag{3}$$

In practice, we fine-tune the positions of the lenses to achieve a magnification of unity, as described later.

To facilitate repositioning the trap, we place a mirror (M1) in the Fourier plane of the trap before lens L1. Tilting M1 then displaces the beam after L1 without changing its direction, as shown in Fig. 1(c), allowing the beam to be moved over a larger range without leaving the aperture of the downstream optics. In principle, M1 can be a galvo-driven mirror [34] or replaced with an acousto-optic deflector [35,36,45] to allow real-time transport of the cloud of atoms in the trap. For this demonstration, we adjust M1 manually and show that the trap remains self-aligned, as illustrated in Fig. 2.

Unlike the vertical behavior, horizontal displacement of the first-pass beam with $A = 1$ causes the opposite movement of the second-pass beam in the vacuum chamber. Under a pure horizontal displacement, the beams stay in the same plane and remain intersected. The crossed trap then moves along its longitudinal axis (z'), as illustrated in Fig 1(d), by a displacement $\Delta z' = \Delta x / \sin(\alpha/2)$. Here Δx is the displacement of the first-pass beam focus in the object coordinate system. The primed coordinates refer to the principle axes of the trap and are related to the object coordinates by a rotation of $\pi - \alpha/2$ about y. For a situation requiring large displacements in both the vertical and horizontal directions, one can set $C = 0$ using $d_1 + d_2 = 2(f_2 + f_3)$. However, in our case, we prefer a

shorter path length for a simpler setup and choose d_1 and d_2 to be smaller than $f_2 + f_3$.

One might ask whether it is necessary to introduce the intermediate image plane in order to achieve a positive magnification ($A > 0$). Given the mirror arrangement shown in Fig. 1(a), no choice of lenses can produce a positive magnification without introducing an intermediate focus, as shown in the Appendix.

In our implementation, the focal lengths of the lenses shown in Fig. 1 are $f_1 = 250\,\text{mm}$, $f_2 = 350\,\text{mm}$, and $f_3 = 150\,\text{mm}$. Lenses L1–L5 are plano-convex spherical singlets of 25.4-mm diameter. The distance between L2 and L3 is $d_1 = 133$ mm, and that between L4 and L5 is $d_2 = 127$ mm. The crossing angle is $\alpha = 3.5°$. A collimated beam of about 2-mm $1/e^2$ intensity radius enters the system at M1.

III. NUMERICAL-RAY-TRACE ANALYSIS

Numerical ray tracing gives the predicted tuning range of the trap in the vertical direction. We employ the OSLO software program to assess the effects of finite lens aperture and geometric aberrations, which are not included in the paraxial model described above. The simulation models a Gaussian beam using a Gaussian distribution of rays in which the central (reference) ray passes through the object plane at y_{ob} and slope zero, similar to Fig. 1(b). Additional rays fan out from that point to produce a 3-mm $1/e^2$ radius Gaussian spot on the first surface of L2, corresponding to an effective Gaussian beam radius of $w_0 = 40\,\mu\text{m}$ in the object plane. The size of the focus in the actual experimental setup is similar, as detailed in Sec. IV. The lens positions and properties are chosen to match the experimental setup. We fine-tune the lens positions to achieve a magnification of 1, as judged by tracing a ray with $y_{\text{ob}} = 1\,\text{mm}$. We then vary y_{ob} to model the effect of tuning the position of the first-pass beam.

The system performs well in simulation up to about $y_{\text{ob}} = 3\,\text{mm}$, at which point several effects begin to limit the performance. The finite aperture of the lenses imposes one limitation. We aim to keep the beam center at least two $1/e^2$ radii away from the lens apertures, which we take to be 11 mm in radius, to avoid clipping the beam. This necessarily limits y_{ob} to be less than 5 mm to avoid clipping at L2. However, at $y_{\text{ob}} = 3\,\text{mm}$, the beam gets close to the edge of L4, with the rays at twice $1/e^2$ attaining a y coordinate of -10.5 mm. This larger deviation of the rays from the optical axis near L4 can be avoided by using $C = 0$, as described later.

Aberrations cause the position y_{im} of the reference ray in the image plane (i.e., the second-pass focus) to deviate from the center y_{ob} of the first-pass beam. Figure 3(a) shows the deviation $y_{\text{im}} - y_{\text{ob}}$ versus trap position y_{ob}. By symmetry, y_{im} is an odd function of y_{ob}, so to third order,

$$y_{\text{im}} = A y_{\text{ob}} + \sigma y_{\text{ob}}^3. \tag{4}$$

The constant σ contains contributions from all five third-order Seidel coefficients. Fitting to the simulation results gives $\sigma = 7 \times 10^{-4}\ \text{mm}^{-2}$. The tuning procedure based on setting $y_{\text{im}} = y_{\text{ob}}$ at $y_{\text{ob}} = 1\,\text{mm}$ technically results in $A \approx 1 - \sigma \times (1\,\text{mm})^2$; however, the difference is negligible.

We aim to keep $|y_{\text{im}} - y_{\text{ob}}|$ less than $0.45 w_0$. In the absence of additional broadening of the second-pass focus, this amount of offset of the beams will result in a 10% reduction in trap depth for the crossed trap, a 15% reduction of the vertical trap frequency, and a 5% reduction in the two horizontal trap frequencies. At $y_{\text{ob}} = 3\,\text{mm}$, we find $y_{\text{im}} - y_{\text{ob}} = 17\,\mu\text{m}$, or $0.43 w_0$, close to the desired limit.

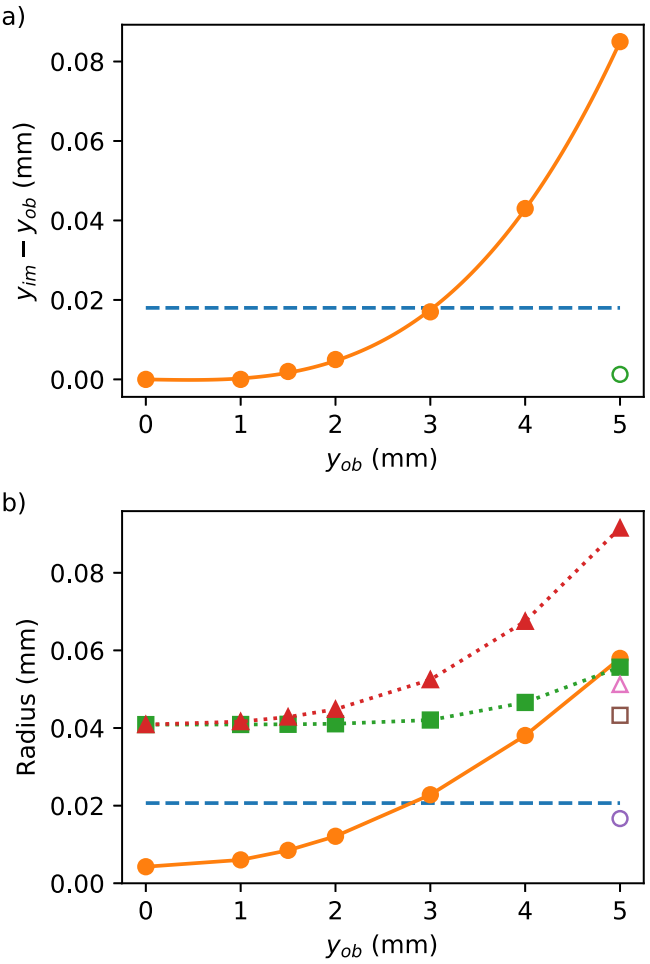

FIG. 3. Numerical simulation. (a) Misalignment $y_{\text{im}} - y_{\text{ob}}$ due to geometric aberration. As in the text, y_{ob} is the vertical position of the reference ray (i.e., the beam center) in the object plane, and y_{im} is the position of the reference ray when it reaches the image plane. Solid circles show the numerical simulation using the parameters of our experimental setup. The curve is from a fit to Eq. (4). The dashed line indicates the value $0.45 w_0 = 18\,\mu\text{m}$ for reference, as discussed in text. The open circle shows $y_{\text{im}} - y_{\text{ob}}$ for a setup where $d_1 = d_2 = f_2 + f_3$, giving $C = 0$ in (3), showing that even at the most extreme end of the range ($y_{\text{ob}} = 5\,\text{mm}$), the misalignment is negligible. (b) Resolution and beam sizes. Solid circles show the geometric rms radius in the image plane. The dashed line shows the Airy disk radius. Solid squares and solid triangles show the beam size as $1/e^2$ semidiameters in the image plane along $\bar{x}$ and $\bar{y}$ axes, respectively, from the diffraction integral. Open symbols show the same quantities as the corresponding solid shapes, but for the $C = 0$ setup.

Geometric aberration due to large y_{ob} can also degrade the trap by broadening the beam focus in the image plane. Figure 3(b) shows the root-mean-square (rms) spot size from geometric ray tracing. For $y_{\text{ob}} = 0$, ray tracing predicts a diffraction-limited spot with a geometric rms radius of about

4 μm. The geometric rms spot size increases with increasing y_{ob} and exceeds the Airy disk radius for y_{ob} greater than about 3 mm. Figure 3(b) also shows that the total beam size at the focus, including both diffraction and geometric aberration, begins to increase noticeably around $y_{ob} = 3$ mm. Due to the symmetry of the system, the position can also be tuned in the opposite direction down to $y_{ob} = -3$ mm. In summary, ray tracing indicates that the trap in our setup can be tuned by ±3 mm for a 6-mm travel range while staying self-aligned and well focused.

We also investigated a hypothetical setup in which the distances d_1 and d_2 are chosen to make $C = 0$ in (3). The results, shown by the open points in Fig. 3, indicate that the system performs well throughout the full range of ±5 mm. At that point, the system is limited by the aperture of the lenses and is also close to no longer being diffraction limited. Remarkably, the position error $y_{im} - y_{ob}$ remains negligible, at about 1 μm.

To generalize our analysis to other values of the waist size w_0, we first calculate the range of motion set by the lens apertures as a function of w_0. As before, we require that the beam center remains at least two beam radii away from the lens apertures. Typically, the lenses sit in the far field of the beam focus, so the size of the beam at any given lens varies inversely with w_0. Therefore, increasing w_0 increases the range of motion. In our setup, $f_2 > f_1$, so the beam is larger at L2 than at L1, and the aperture of L2 imposes an upper bound on the vertical trap displacement y_{max} of

$$y_{max} = R_L - \frac{2}{w_0}\sqrt{\left(\frac{f_2\lambda}{\pi}\right)^2 + w_0^4}, \tag{5}$$

where λ is the laser wavelength and R_L is the clear aperture radius of the lenses. The first term in the square root dominates in the far field ($f_2 > \pi w_0^2/\lambda$), confirming that the range of motion increases with w_0, as shown in Fig. 4. Eventually, for large w_0 (beyond the domain shown in Fig. 4), the range of motion decreases due to the increased beam size in the near field.

While L2 provides the limiting aperture when $C = 0$ (and $f_2 > f_1, f_3$), L4 imposes a smaller limit as d_1 and d_2 are reduced away from $C = 0$, as in our setup. Using the paraxial approximation to calculate the position and size of the beam at L4 and applying the distances and focal lengths for our setup, we find that L4 allows a maximum trap displacement of

$$y_{max} = R_L - 3.55\,\text{mm} - \frac{2}{w_0}\sqrt{(0.283\,\text{mm})^4 + w_0^4}. \tag{6}$$

We note that Eq. (6) for L4 retains a dependence on w_0 similar to Eq. (5) for L2.

To understand how changing w_0 affects the limits imposed by geometric aberrations, we first note that the results shown in Fig. 3(a) for aberration-induced misalignment versus trap position hold equally for all values of w_0, as they are based on tracing the central ray. However, the desired degree of alignment depends on w_0, set by the condition $|y_{im} - y_{ob}| < 0.45w_0$. Combining this inequality with Eq. (4) shows that the travel-range limit imposed by misalignment is $y_{max} = (0.45w_0/\sigma)^{1/3}$. As shown in Fig. 4, this becomes the limiting condition in our setup for waist sizes greater than about 45 μm.

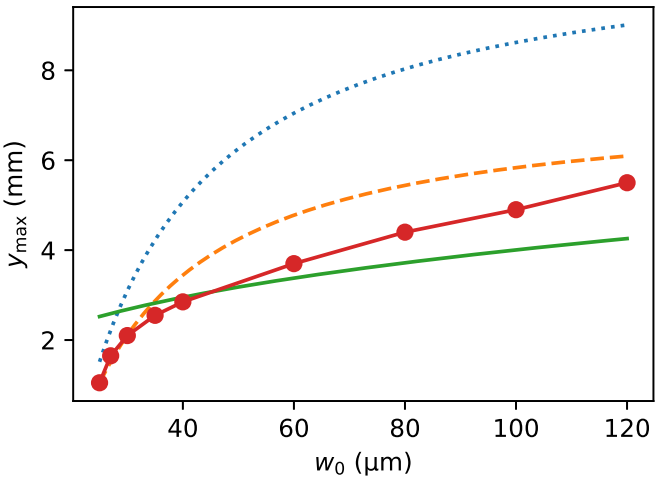

FIG. 4. Upper bounds on the range of motion of the self-aligning crossed ODT versus the beam-waist size. Blue dots (orange dashes): limit set by the aperture of lens L2 (L4), assuming a clear aperture radius of $R_L = 11$ mm. Red circles: limit set by requiring a diffraction-limited second-pass focus. Green curve: limit set by requiring less than $0.45w_0$ of misalignment. The range of motion is $\pm y_{max}$, where y_{max} is the least of the upper bounds for a given w_0. The bound set by the aperture of L2 (blue dots) becomes the limiting factor when $d_1 = d_2 = f_2 + f_3$, giving $C = 0$ in (3), as the other bounds become less stringent in that case.

We also include in Fig. 4 the range limit imposed by requiring that the second-pass focus remain diffraction limited, determined from OSLO simulations. Finally, for a hypothetical setup where $d_1 = d_2 = f_2 + f_3$, setting $C = 0$ in (3), we find that geometric aberrations become far less significant, so that the limit imposed by the aperture of L2 (5) determines the full range of motion.

IV. EXPERIMENTAL SETUP

Light for the optical dipole trap comes from a linearly polarized 200-W IPG Photonics fiber laser at 1064-nm wavelength (linewidth of about 3 nm), which we operate at 70% power. The power is stabilized and controlled using an acousto-optic modulator (AOM; Gooch & Housego AOMO 3110-197). Transmission through a polarizing beam-splitter plate before M1 ensures pure horizontal polarization. A half-wave plate on the second pass rotates the polarization to the vertical to prevent interference with the first-pass beam. Light transmitted through a backside-polished mirror (M2) is sent to a photodiode for stabilization. The first- and second-pass beams have respective $1/e^2$ intensity waist radii of $(w_{1x}, w_{1y}) = (47(1)\,\mu\text{m}, 33(1)\,\mu\text{m})$ and $(w_{2\bar{x}}, w_{2\bar{y}}) = (51(4)\,\mu\text{m}, 41(4)\,\mu\text{m})$ and maximum optical powers of 78 and 74 W. For these parameters, gravitational sag of lithium atoms is expected to be negligible (<1 nm).

We test our setup by loading ^{6}Li atoms into the crossed ODT from a laser-cooled cloud. First, a magneto-optical trap (MOT) on the D_2 line collects about 5×10^8 atoms in 5 s from a Zeeman-slowed atomic beam. The ODT light is applied to the cloud during the final 2 s of MOT loading to minimize the effects of thermal lensing by allowing the optics to reach

a steady temperature. The MOT employs three retroreflected beams of red-detuned cooling and repumping light, with powers of 12 and 3.1 mW per beam, respectively, and beam diameters of about 10 mm. The MOT quadrupole magnetic field produces a 32 G/cm gradient in the axial direction. Small bias fields (< 10 G) control the MOT position. The MOT has a temperature of about 2 mK. To reduce the temperature to 500 μK and increase the density, we apply a compressed MOT (cMOT) phase for 5 ms by reducing the cooling and repumping light detunings from -35 and -27 MHz, respectively, to -10 MHz each, while reducing their intensity to 1%–2% of their initial values. The magnetic field gradient is kept constant. The Zeeman slower coils are shut off after the first 3 ms of the cMOT phase, together with the bias field along the Zeeman slower axis. At the end of the cMOT phase, we switch off the remaining bias fields and the MOT quadrupole magnetic field. The cooling and repumping light remain on for a 0.1-ms dwell time before proceeding with gray-molasses cooling.

Gray-molasses cooling on the D_1 line [31] is applied for 1.5 ms after the compressed MOT dwell time and brings the temperature down to about 150 μK. To deliver D_1 light to the apparatus, we combine four beams, the D_1 and D_2 cooling and repumping beams, on a 4×4 fiber splitter array. Three output fibers are used for the three axes of cooling, and the fourth output is used as a monitor. The D_1 cooling and repumping beams have 13 and 1.1 mW of power per beam and are blue detuned by 25 MHz from the $F = 3/2$ to $F' = 3/2$ and $F = 1/2$ to $F' = 3/2$ transitions, respectively.

After extinguishing the gray-molasses light, we optically pump atoms into the $F = 1/2$ ground-state manifold. Atoms not held in the crossed ODT now fly away freely. We ramp up a magnetic field in the vertical direction to 286 G over 15 ms and hold the cloud for 500 ms to allow equilibration. Atoms then occupy the two lowest hyperfine states, $|1\rangle$ and $|2\rangle$. We primarily image state $|2\rangle$ via absorption of a 10-μs pulse of resonant light. To image state $|1\rangle$, we instead ramp to 338 G, using the same light frequency. For most purposes, we image along an axis in the horizontal plane at 45° to the first-pass ODT beam using horizontal linear polarization. A second imaging system operates in the vertical direction to visualize the beam crossing as in Fig. 2(a).

V. TESTING THE SELF-ALIGNING TRAP WITH ^{6}Li ATOMS

A. Tuning to unity magnification

Before testing the self-aligning performance of the trap, we tuned the positions of lenses L4 and L5 through an iterative procedure to bring the magnification to 1. We first aligned the two foci of the crossed trap, with the help of images of the trapped atoms. We then moved the first-pass focus in the vertical (y) direction by about a millimeter and loaded atoms into the ODT. At first, the magnification was sufficiently far from 1 that the beams no longer overlapped afterward, and we could see two separate atomic clouds. From images of the two clouds, we determined the positions $y_{\rm ob}$ and $y_{\rm im}$ of the first- and second-pass foci, respectively, giving the magnification $M \equiv y_{\rm im}/y_{\rm ob}$ at that step of iteration. To improve the magnification, we adjusted positions z_4 and z_5 of lenses L4 and L5 based on a ray-optics calculation. Theoretically, the derivative dA/dz_4 of the paraxial magnification with respect to the position of lens L4 and subject to the constraint that lens L5 is simultaneously adjusted to keep the image plane fixed is $dA/dz_4 = -0.017\,\mathrm{mm}^{-1}$; meanwhile, $dz_5/dz_4 = 4.4$. Using these derivatives, we estimated the displacements dz_4 and dz_5 needed to bring the magnification to 1 without shifting the focus. After applying the adjustments and fine-tuning L5 using the atoms to correct any remaining offset in the axial position of the focus, we measured the magnification again, then adjusted L4 and L5 a second, and final, time.

After the second update of L4 and L5, moving the trap from its central, aligned position to the new position $y_{\rm ob} = 1.7$ mm produced no visible splitting of the atomic density distribution versus y, indicating that the two foci moved by the same amount to within about a beam radius. To measure the magnification at that point, we applied a different procedure to detect the misalignment $y_{\rm im} - y_{\rm ob}$ with precision finer than the atomic cloud size. We measured the small misalignment by relaying the second-pass focus onto an auxiliary camera, using a sample of the trap light transmitted by a backside-polished mirror. We measured positions $\tilde{y}_1$ and $\tilde{y}_2$ of the beam center on the auxiliary camera before and after moving the first-pass beam to $y_{\rm ob}$. We then intentionally misaligned the second-pass beam in the vertical direction using M3, enough to create two separate optical traps. We measured the vertical displacement dy between the two atomic cloud centers versus the position $\tilde{y}$ of the beam on the auxiliary camera as we scanned M3. A linear fit then gave the value $\tilde{y}_3$ at which $dy = 0$. The value $\tilde{y}_3$ identifies the position of the first-pass focus in the coordinate system of the auxiliary camera. Therefore, $y_{\rm ob} \propto \tilde{y}_3 - \tilde{y}_1$, and $y_{\rm im} \propto \tilde{y}_2 - \tilde{y}_1$. Finally, the magnification of the self-aligning crossed ODT is given by $M = (\tilde{y}_2 - \tilde{y}_1)/(\tilde{y}_3 - \tilde{y}_1)$. In the final configuration, the magnification was indistinguishable from 1. Using $y_{\rm ob} = -1.7$ mm gave $M = 0.995$, and using $y_{\rm ob} = 1.7$ mm gave $M = 1.004$, which we summarize as $M = 1.000(5)$.

B. Evaluation of self-aligning performance

To evaluate the performance of the self-aligning crossed ODT, the trap is tuned over a range of positions along the vertical direction using mirror M1. At each trap position, we adjust the vertical MOT bias field to center the laser-cooled cloud on the crossed ODT and maximize the number of atoms transferred. The trap is evaluated by measuring the loading efficiency and the transverse trapping frequency at each position.

The location of the crossed ODT was adjusted over a vertical range of 4.3 mm. Figure 2(b) shows images of the trapped cloud at each of six positions tested, demonstrating qualitatively that the trap remains aligned. To determine the loading efficiency, the atom populations of the gray-molasses cloud and the crossed ODT were measured at each position. The loading efficiency is shown in Fig. 5. On average, we obtain 3×10^8 atoms in the gray-molasses cloud and 7.5×10^5 atoms in the crossed ODT, for an average loading efficiency of 2.5×10^{-3}. For vertical positions beyond -2 mm, the atom population in both traps decreases due to the reduction in

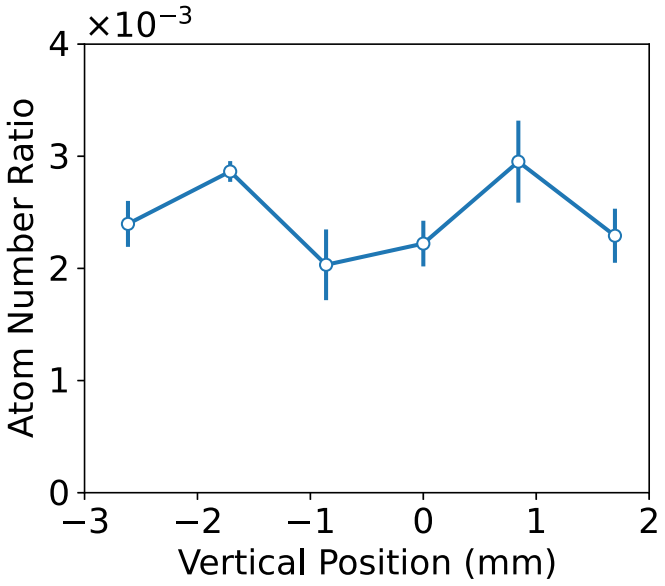

FIG. 5. Fraction of atoms transferred from gray molasses to the crossed ODT vs the position of the ODT. The gray molasses is also moved to match the ODT location by adjusting the vertical bias field.

the MOT atom number. In the other direction, the travel range is limited by the lens apertures due to imperfect lens centering. However, the loading efficiency stays relatively constant throughout the range measured, demonstrating the self-aligning property of the crossed ODT.

The trap frequencies serve as another indicator of alignment. Transverse trap frequencies were measured at each ODT position by parametric heating at a magnetic field of 286 G and are shown in Fig. 6(a). The ODT optical power was modulated sinusoidally by applying 800 cycles of amplitude modulation to the AOM rf drive. The average optical power in the first-pass beam was reduced to 68 W for better linearity, with a modulation amplitude of 1.1 W. At this magnetic field, temperature, and density, the gas is in the nearly collisionless, classical regime in a nearly harmonic potential, where its collective-mode frequencies are integer multiples of the trap frequencies ν_i [52–54]. Parametric resonances are expected at $2\nu_i$ and subharmonics [55].

Parametric heating of the cloud is detected by measuring the cloud size after 0.1-ms time of flight, which gives greater sensitivity than measuring atom loss [55]. A typical modulation spectrum is shown in Fig. 6(b). The resonances correspond to $2\nu_i$ for the two transverse trap frequencies. Due to the ellipticity of the trapping beams, the transverse trap frequencies are several kilohertz apart. We extract the peak positions by fitting the spectra to a sum of two Gaussians. The highest trap frequencies obtained for the two transverse axes are $\nu_x = 13.6$ kHz and $\nu_y = 20.4$ kHz. We also observed a parametric resonance near 1 kHz corresponding to twice the axial frequency.

As shown in Fig. 5(a), the transverse trap frequencies decrease by about 7% each across the range of trap positions. In comparison, the amount of vertical misalignment that would lead to a 10% reduction in trap depth, including the beam ellipticities, would cause reductions by 7% and 13%,

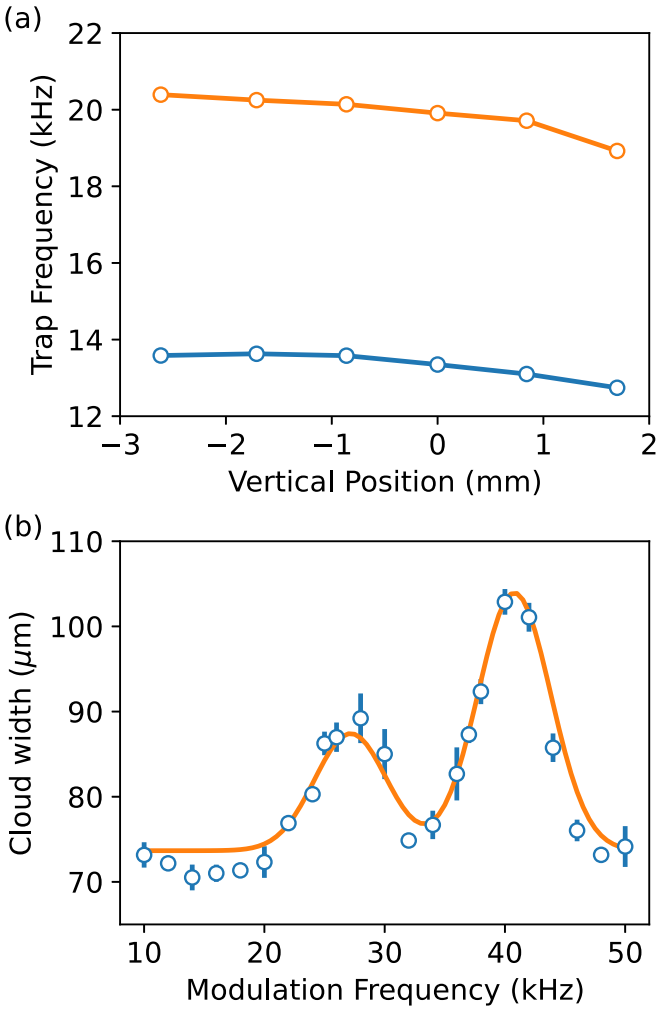

FIG. 6. (a) Transverse trap frequencies as a function of ODT position. (b) Typical modulation spectrum, showing cloud size (one standard deviation of the vertical density distribution) after 0.1-ms time of flight. The peaks correspond to 2 times the transverse trap frequencies.

respectively, in the trap frequencies. The trap frequencies stay above this threshold, indicating that the crossed ODT remains well aligned to within the desired specifications.

C. Evaluation of trap stability

In a crossed ODT, interference between the two trapping beams poses a potential source of heating. Previous work employing similar high-power lasers to form crossed dipole traps found that the use of orthogonal linear polarizations for the two beams provides an effective means to suppress interference and heating [28,48–50]. We confirm the effectiveness of using orthogonal linear polarizations to inhibit interference in our setup by comparing the lifetime of atoms in the crossed ODT to the lifetime in a single-beam ODT. To measure the lifetime in the crossed trap, we first ramp the trap beam power down to 4.4 W over 2.3 s at a magnetic bias field of 338 G, bringing the cloud temperature down to 9 μK. After waiting 2 s to allow for equilibration through plain evaporation, we apply a variable wait time and measure the

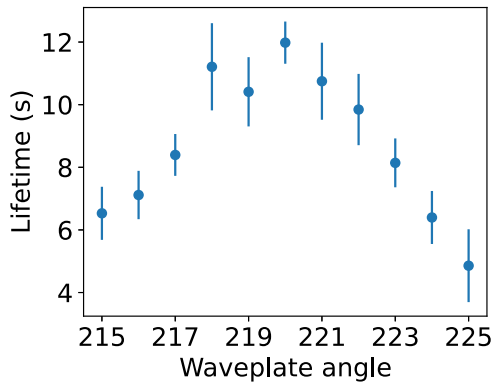

FIG. 7. Lifetime $(1/e)$ of atoms in the crossed ODT vs the angle of the half-wave plate on the second-pass path, showing that the heating due to interference between the two trapping beams can be minimized by using orthogonal polarizations. The trap power is ramped down to 4.4 W before the lifetime measurement. The wave-plate angle is measured in degrees relative to an arbitrary zero.

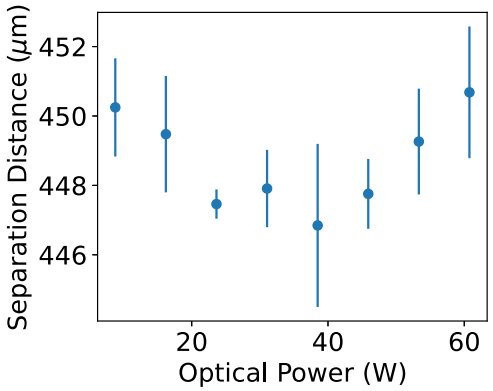

FIG. 8. The two trapping beam foci are intentionally separated by 450 μm in the vertical direction to measure their relative positions versus trap power. The relative change in position is less than about 4 μm, significantly less than the beam-waist sizes.

atom number through absorption imaging. Figure 7 shows the lifetime of atoms in the trap versus the angle of the half-wave plate on the second-pass path. The lifetime reaches a peak of 12.0(7) s when the second-pass polarization is orthogonal to that of the first pass. Lifetimes on the order of 10 s are typical for experiments on optically trapped lithium atoms (see, e.g., [28,56]).

To assess the possibility of residual heating due to imperfect polarization, we compare the lifetime in the crossed ODT to the lifetime in a single-beam ODT, where interference will not occur. To measure the single-beam trap lifetime, we misalign the two beams by about 450 μm, capture atoms in the two separated traps, and ramp the power to 8.8 W to achieve a maximum optical intensity similar to the crossed-beam measurement. In the single-beam case, we find a lifetime of 10(1) s, slightly less than the lifetime of the crossed trap at the optimal wave-plate angle. Interference in the crossed-beam trap therefore does not pose a significant source of heating and trap loss.

To gauge the effect of thermal lensing on the alignment of the crossed trap, we measure the change in relative position of the two trapping beams versus optical power. Like in the procedure for the single-beam lifetime measurement, we separate the two passes by 450 μm in the vertical direction. We then ramp the power over a fixed time to a variable final value ranging from 8.8 to 62 W. Figure 8 shows the distance between the cloud centers as a function of the final laser power. The relative position of the beams varies by about 4 μm, or about 10% of the beam waist, and therefore does not significantly affect the alignment of the crossed trap.

As a final point, we note that the self-aligning configuration greatly improved the trap stability in daily use compared to a conventional configuration with negative vertical magnification. This suggests that the dominant source of alignment drift in this setup comes from the first-pass beam, possibly due to strong thermal lensing in the AOM [57]. We therefore find this setup advantageous even when the trap does not need to be repositioned dynamically.

VI. CONCLUSION

We demonstrated a self-aligning crossed optical dipole trap using a recirculated trapping beam in an approximately horizontal plane. The presence of an intermediate focus gives a positive lateral magnification of the overlapping foci. Tuning the vertical magnification to 1.000(5) yielded a self-aligning configuration, in which the foci remain overlapped as the first focus was moved in the vertical direction. Numerical ray tracing predicted that this scheme works well even in the presence of geometric aberration. We confirmed these predictions by loading ^{6}Li atoms into the trap throughout a 4.3-mm range of trap positions and observing robust atom loading and trap frequencies without requiring any realignment to account for the position change.

The self-aligning property increases the stability of the recirculated crossed ODT and provides the ability to transport the trapped atoms if required. Our numerical-ray-tracing analysis predicts that the travel range of the trap can be extended further with a slight variation on the setup (using $C = 0$) and by using optical components with larger apertures. In the context of dynamic positioning, we envision this method being useful for bringing atoms in a recirculated crossed ODT close to a surface. Lateral movement of the trap position would allow bringing the sample to within a few times the beam waist, typically tens of microns, from a surface without subjecting the surface to the trapping beams. This could be used in field sensing from surfaces with cold-atom sensors or to evaporatively cool a cloud of atoms to quantum degeneracy before transporting it to the vicinity of a hollow-core fiber for quantum optics applications.

ACKNOWLEDGMENTS

We would like to thank several current and former undergraduate students who contributed to constructing components of the apparatus used in this work: E. Shen; A. Lemmon; G. Awad; and REU students J. Chen, C. Brady, and M. K. Pasha (NSF REU Site Award No. 1852010). This work was supported by the National Science Foundation (Award No. 2110483) and a Lehigh University Faculty Innovation Grant (Grant No. FIGAWD274). M.M.-M. acknowledges

support from a Lee Fellowship through the Lehigh University Physics Department.

APPENDIX: NECESSITY OF AN INTERMEDIATE FOCUS

Our optical system achieves a positive magnification by producing an intermediate focus partway through the imaging system. Is it possible to achieve a positive magnification without an intermediate image plane? Here we show that the intermediate focal plane is required in a system where the optical axis lies within a single plane (the horizontal plane in our system).

We consider the vertical component of the paraxial rays. The ray transfer matrix relates the input and output rays of the optical system:

$$\begin{pmatrix} y_f \\ \theta_f \end{pmatrix} = \begin{pmatrix} A & B \\ C & D \end{pmatrix} \begin{pmatrix} y_i \\ \theta_i \end{pmatrix}. \tag{A1}$$

The condition $B = 0$ ensures that the system images rays from a given point in the input (object) plane to a single point in the output (image) plane regardless of their angle. A classical optical system (composed, for example, of lenses, mirrors, and free-space propagation) has the property [58]

$$AD - BC = n/n', \tag{A2}$$

where n and n' are the indices of refraction of the medium in the input and output planes, respectively. This condition expresses conservation of phase-space volume and relates to the concept of the optical invariant. In our case, $n' = n$, $B = 0$, $A = M$ (lateral magnification), and $D = M_\gamma$ (angular magnification), giving

$$MM_\gamma = 1. \tag{A3}$$

A ray starting at $y_i = 0$ and arbitrary positive angle $\theta_i > 0$ will enter the lens system with positive position $y_1 > 0$. By definition, this ray will cross the optical axis at any image plane because it started at $y_i = 0$. If no intermediate image plane occurs, this ray never crosses the optical axis within the lens system and must exit with $y > 0$. Therefore, approaching the final focus, this ray will have a negative final angle $\theta_f < 0$. The angular magnification $M_\gamma = \theta_f/\theta_i$ is therefore negative, and the lateral magnification M must also be negative. Therefore, a lens system with no internal image planes and a planar optical axis will have a negative magnification in the direction perpendicular to the plane containing the optical axis.

To achieve positive magnification (relative to a fixed axis) without introducing an intermediate image plane, one could employ a nonplanar optical path. In particular, one can leverage the inversion of the axis that lies within the plane of incidence upon reflection from a mirror, as in a telescope star diagonal.

[1] W. S. Bakr, J. I. Gillen, A. Peng, S. Fölling, and M. Greiner, A quantum gas microscope for detecting single atoms in a Hubbard-regime optical lattice, Nature (London) **462**, 74 (2009).

[2] M. Miranda, A. Nakamoto, Y. Okuyama, A. Noguchi, M. Ueda, and M. Kozuma, All-optical transport and compression of ytterbium atoms into the surface of a solid immersion lens, Phys. Rev. A **86**, 063615 (2012).

[3] L. W. Cheuk, M. A. Nichols, M. Okan, T. Gersdorf, V. V. Ramasesh, W. S. Bakr, T. Lompe, and M. W. Zwierlein, Quantum-gas microscope for fermionic atoms, Phys. Rev. Lett. **114**, 193001 (2015).

[4] Y. Long, F. Xiong, and C. V. Parker, Spin susceptibility above the superfluid onset in ultracold Fermi gases, Phys. Rev. Lett. **126**, 153402 (2021).

[5] C. Shkedrov, M. Menashes, G. Ness, A. Vainbaum, E. Altman, and Y. Sagi, Absence of heating in a uniform Fermi gas created by periodic driving, Phys. Rev. X **12**, 011041 (2022).

[6] F. J. Vivanco, A. Schuckert, S. Huang, G. L. Schumacher, G. G. T. Assumpção, Y. Ji, J. Chen, M. Knap, and N. Navon, The strongly driven Fermi polaron, arXiv:2308.05746

[7] M. Greiner, I. Bloch, T. W. Hänsch, and T. Esslinger, Magnetic transport of trapped cold atoms over a large distance, Phys. Rev. A **63**, 031401(R) (2001).

[8] T. L. Gustavson, A. P. Chikkatur, A. E. Leanhardt, A. Görlitz, S. Gupta, D. E. Pritchard, and W. Ketterle, Transport of Bose-Einstein condensates with optical tweezers, Phys. Rev. Lett. **88**, 020401 (2001).

[9] C. Gross, H. C. J. Gan, and K. Dieckmann, All-optical production and transport of a large ^{6}Li quantum gas in a crossed optical dipole trap, Phys. Rev. A **93**, 053424 (2016).

[10] J. H. Lee, H. Jung, J.-Y. Choi, and J. Mun, Transporting cold atoms using an optically compensated zoom lens, Phys. Rev. A **102**, 063106 (2020).

[11] T. Klostermann, C. R. Cabrera, H. von Raven, J. F. Wienand, C. Schweizer, I. Bloch, and M. Aidelsburger, Fast long-distance transport of cold cesium atoms, Phys. Rev. A **105**, 043319 (2022).

[12] M. Seo, I. H. Do, H. Lee, D.-H. Yu, S. Seo, H.-G. Hong, J. H. Han, S. E. Park, S.-B. Lee, T. Y. Kwon, J. Mun, and J. H. Lee, Moving-frame imaging of transiting cold atoms for precise long-range transport, Opt. Express **30**, 25707 (2022).

[13] Y. Bao, S. S. Yu, L. Anderegg, S. Burchesky, D. Gonzalez-Acevedo, E. Chae, W. Ketterle, K.-K. Ni, and J. M. Doyle, Fast optical transport of ultracold molecules over long distances, New J. Phys. **24**, 093028 (2022).

[14] A. J. Matthies, J. M. Mortlock, L. A. McArd, A. P. Raghuram, A. D. Innes, P. D. Gregory, S. L. Bromley, and S. L. Cornish, Long-distance optical-conveyor-belt transport of ultracold ^{133}Cs and ^{87}Rb atoms, Phys. Rev. A **109**, 023321 (2024).

[15] N. Behbood, F. Martin Ciurana, G. Colangelo, M. Napolitano, M. W. Mitchell, and R. J. Sewell, Real-time vector field tracking with a cold-atom magnetometer, Appl. Phys. Lett. **102**, 173504 (2013).

[16] Y. Cohen, K. Jadeja, S. Sula, M. Venturelli, C. Deans, L. Marmugi, and F. Renzoni, A cold atom radio-frequency magnetometer, Appl. Phys. Lett. **114**, 073505 (2019).

[17] A. Facon, E.-K. Dietsche, D. Grosso, S. Haroche, J.-M. Raimond, M. Brune, and S. Gleyzes, A sensitive electrometer based on a Rydberg atom in a Schrödinger-cat state, Nature (London) **535**, 262 (2016).

[18] P. Krüger, S. Wildermuth, S. Hofferberth, L. M. Andersson, S. Groth, I. Bar-Joseph, and J. Schmiedmayer, Cold atoms close to surfaces: Measuring magnetic field roughness and disorder potentials, J. Phys.: Conf. Ser. **19**, 56 (2005).

[19] F. Sorrentino, A. Alberti, G. Ferrari, V. V. Ivanov, N. Poli, M. Schioppo, and G. M. Tino, Quantum sensor for atom-surface interactions below 10μm, Phys. Rev. A **79**, 013409 (2009).

[20] J. A. Sauer, K. M. Fortier, M. S. Chang, C. D. Hamley, and M. S. Chapman, Cavity QED with optically transported atoms, Phys. Rev. A **69**, 051804(R) (2004).

[21] J. Ningyuan, A. Georgakopoulos, A. Ryou, N. Schine, A. Sommer, and J. Simon, Observation and characterization of cavity Rydberg polaritons, Phys. Rev. A **93**, 041802(R) (2016).

[22] A. Kumar, A. Suleymanzade, M. Stone, L. Taneja, A. Anferov, D. I. Schuster, and J. Simon, Quantum-enabled millimetre wave to optical transduction using neutral atoms, Nature (London) **615**, 614 (2023).

[23] T. Peters, L. P. Yatsenko, and T. Halfmann, Loading and spatially resolved characterization of a cold atomic ensemble inside a hollow-core fiber, Phys. Rev. A **103**, 063302 (2021).

[24] Y. Wang, S. Chai, T. Billotte, Z. Chen, M. Xin, W. S. Leong, F. Amrani, B. Debord, F. Benabid, and S.-Y. Lan, Enhancing fiber atom interferometer by in-fiber laser cooling, Phys. Rev. Res. **4**, L022058 (2022).

[25] Y. Song, W. Li, X. Xu, R. Han, C. Gao, C. Dai, and N. Song, Tightly trapped atom interferometer inside a hollow-core fiber, Photonics **11**, 428 (2024).

[26] M. D. Barrett, J. A. Sauer, and M. S. Chapman, All-optical formation of an atomic Bose-Einstein condensate, Phys. Rev. Lett. **87**, 010404 (2001).

[27] T. Kinoshita, T. Wenger, and D. S. Weiss, All-optical Bose-Einstein condensation using a compressible crossed dipole trap, Phys. Rev. A **71**, 011602(R) (2005).

[28] J. Fuchs, G. J. Duffy, G. Veeravalli, P. Dyke, M. Bartenstein, C. J. Vale, P. Hannaford, and W. J. Rowlands, Molecular Bose–Einstein condensation in a versatile low power crossed dipole trap, J. Phys. B **40**, 4109 (2007).

[29] J.-F. Clément, J.-P. Brantut, M. Robert-de Saint-Vincent, R. A. Nyman, A. Aspect, T. Bourdel, and P. Bouyer, All-optical runaway evaporation to Bose-Einstein condensation, Phys. Rev. A **79**, 061406(R) (2009).

[30] P. M. Duarte, R. A. Hart, J. M. Hitchcock, T. A. Corcovilos, T.-L. Yang, A. Reed, and R. G. Hulet, All-optical production of a lithium quantum gas using narrow-line laser cooling, Phys. Rev. A **84**, 061406(R) (2011).

[31] A. Burchianti, G. Valtolina, J. A. Seman, E. Pace, M. De Pas, M. Inguscio, M. Zaccanti, and G. Roati, Efficient all-optical production of large ^{6}Li quantum gases using D_1 gray-molasses cooling, Phys. Rev. A **90**, 043408 (2014).

[32] A. H. Hansen, A. Khramov, W. H. Dowd, A. O. Jamison, V. V. Ivanov, and S. Gupta, Quantum degenerate mixture of ytterbium and lithium atoms, Phys. Rev. A **84**, 011606(R) (2011).

[33] K. M. O'Hara, S. L. Hemmer, M. E. Gehm, S. R. Granade, and J. E. Thomas, Observation of a strongly interacting degenerate Fermi gas of atoms, Science **298**, 2179 (2002).

[34] A. Lengwenus, J. Kruse, M. Schlosser, S. Tichelmann, and G. Birkl, Coherent transport of atomic quantum states in a scalable shift register, Phys. Rev. Lett. **105**, 170502 (2010).

[35] M. Endres, H. Bernien, A. Keesling, H. Levine, E. R. Anschuetz, A. Krajenbrink, C. Senko, V. Vuletic, M. Greiner, and M. D. Lukin, Atom-by-atom assembly of defect-free one-dimensional cold atom arrays, Science **354**, 1024 (2016).

[36] D. Barredo, S. d. Léséleuc, V. Lienhard, T. Lahaye, and A. Browaeys, An atom-by-atom assembler of defect-free arbitrary two-dimensional atomic arrays, Science **354**, 1021 (2016).

[37] D. Stuart and A. Kuhn, Single-atom trapping and transport in DMD-controlled optical tweezers, New J. Phys. **20**, 023013 (2018).

[38] T. M. Graham *et al.*, Multi-qubit entanglement and algorithms on a neutral-atom quantum computer, Nature (London) **604**, 457 (2022).

[39] J. Léonard, M. Lee, A. Morales, T. M. Karg, T. Esslinger, and T. Donner, Optical transport and manipulation of an ultracold atomic cloud using focus-tunable lenses, New J. Phys. **16**, 093028 (2014).

[40] G. Unnikrishnan, C. Beulenkamp, D. Zhang, K. P. Zamarski, M. Landini, and H.-C. Nägerl, Long distance optical transport of ultracold atoms: A compact setup using a moiré lens, Rev. Sci. Instrum. **92**, 063205 (2021).

[41] R. Grimm, M. Weidemüller, and Y. B. Ovchinnikov, Optical dipole traps for neutral atoms, Adv. At. Mol. Opt. Phys. **42**, 95 (2000).

[42] T. Bourdel, L. Khaykovich, J. Cubizolles, J. Zhang, F. Chevy, M. Teichmann, L. Tarruell, S. J. J. M. F. Kokkelmans, and C. Salomon, Experimental study of the BEC-BCS crossover region in lithium 6, Phys. Rev. Lett. **93**, 050401 (2004).

[43] R. Anderson, F. Wang, P. Xu, V. Venu, S. Trotzky, F. Chevy, and J. H. Thywissen, Conductivity spectrum of ultracold atoms in an optical lattice, Phys. Rev. Lett. **122**, 153602 (2019).

[44] S.-K. Tung, C. Parker, J. Johansen, C. Chin, Y. Wang, and P. S. Julienne, Ultracold mixtures of atomic ^{6}Li and ^{133}Cs with tunable interactions, Phys. Rev. A **87**, 010702(R) (2013).

[45] Y.-D. Chen, W.-X. Li, Y.-T. Sun, Q.-C. Chen, P.-Y. Chang, and S. Tung, Dual-species Bose-Einstein condensates of ^{7}Li and ^{133}Cs, Phys. Rev. A **108**, 033301 (2023).

[46] J. R. Williams, Universal few-body physics in a three-component Fermi gas, Ph.D. thesis, Pennsylvania State University, 2010.

[47] T. B. Ottenstein, Few-body physics in ultracold Fermi gases, Ph.D. thesis, University of Heidelberg, 2010.

[48] D. Mitra, Exploring attractively interacting fermions in 2D using a quantum gas microscope, Ph.D. thesis, Princeton University, 2018.

[49] T. B. Ottenstein, T. Lompe, M. Kohnen, A. N. Wenz, and S. Jochim, Collisional stability of a three-component degenerate Fermi gas, Phys. Rev. Lett. **101**, 203202 (2008).

[50] T. Lompe, Efimov physics in a three-component Fermi gas, Ph.D. Thesis, University of Heidelberg, 2011.

[51] D. Zhang and A. T. Sommer, Transport of spin and mass at normal-superfluid interfaces in the unitary Fermi gas, Phys. Rev. Res. **4**, 023231 (2022).

[52] D. Guery-Odelin, F. Zambelli, J. Dalibard, and S. Stringari, Collective oscillations of a classical gas confined in harmonic traps, Phys. Rev. A **60**, 4851 (1999).

[53] S. Stringari, Collective excitations of a trapped Bose-condensed gas, Phys. Rev. Lett. **77**, 2360 (1996).

[54] H. Heiselberg, Collective modes of trapped gases at the BEC-BCS crossover, Phys. Rev. Lett. **93**, 040402 (2004).

[55] S. Balik, A. L. Win, and M. D. Havey, Imaging-based parametric resonance in an optical dipole-atom trap, Phys. Rev. A **80**, 023404 (2009).

[56] M. W. Zwierlein, J. R. Abo-Shaeer, A. Schirotzek, C. H. Schunck, and W. Ketterle, Vortices and superfluidity in a strongly interacting Fermi gas, Nature (London) **435**, 1047 (2005).

[57] C. Simonelli, E. Neri, A. Ciamei, I. Goti, M. Inguscio, A. Trenkwalder, and M. Zaccanti, Realization of a high power optical trapping setup free from thermal lensing effects, Opt. Express **27**, 27215 (2019).

[58] R. Guenther, *Modern Optics* (Wiley, New York, 1990).